

Imaging shape and strain in nanoscale engineered semiconductors for photonics by coherent x-ray diffraction

Felisa Berenguer¹, Giorgio Pettinari², Marco Felici ³, Nilanthy Balakrishnan ⁴, Jesse N. Clark^{5,6}, Sylvain Ravy ^{1,7}, Amalia Patané⁴, Antonio Polimeni³ & Gianluca Ciatto ¹✉

Coherent x-ray diffractive imaging is a nondestructive technique that extracts three-dimensional electron density and strain maps from materials with nanometer resolution. It has been utilized for materials in a range of applications, and has significant potential for imaging buried nanostructures in functional devices. Here, we show that coherent x-ray diffractive imaging is able to bring new understanding to a lithography-based nanofabrication process for engineering the optical properties of semiconducting GaAs_{1-y}N_y on a GaAs substrate. This technique allows us to test the process reliability and the manufactured patterns quality. We demonstrate that regular and sharp geometrical structures can be produced on a few-micron scale, and that the strain distribution is uniform even for highly strained sub-microscopic objects. This nondestructive study would not be possible using conventional microscopy techniques. Our results pave the way for tailoring the optical properties of emitters with nanometric precision for nanophotonics and quantum technology applications.

¹Synchrotron SOLEIL, L'Orme des Merisiers, Saint-Aubin, BP48, 91192 Gif-sur-Yvette Cedex, France. ²CNR, Institute for Photonics and Nanotechnologies, Via Cineto Romano 42, 00156 Roma, Italy. ³Department of Physics, Sapienza Università di Roma, Piazzale A. Moro 2, 00185 Roma, Italy. ⁴School of Physics and Astronomy, University of Nottingham, Nottingham NG7 2RD, UK. ⁵Stanford PULSE Institute, SLAC National Accelerator Laboratory, 2575 Sand Hill Road, Menlo Park, CA 94025, USA. ⁶Center for Free-Electron Laser Science (CFEL), Deutsches Elektronensynchrotron (DESY), Notkestrasse 85, 22607 Hamburg, Germany. ⁷Laboratoire de Physique des Solides, CNRS UMR 8502, University of Paris-Sud, Université Paris-Saclay, 91405 Orsay, France. ✉email: gianluca.ciatto@synchrotron-soleil.fr

Full control over size and distribution of semiconductor nanostructures is mandatory for the fabrication of a number of innovative devices, including photonic crystal structures. Nonetheless, the control of the material properties in the growth plane remains challenging. “Top-down” methods based on lithographic processes allow production of highly uniform quantum dot and wire arrays¹. However, these nanostructures often have poor optical properties. High-optical efficiency can be obtained from quantum dots/wires spontaneously formed via self-assembly in highly strained heterostructures (“bottom-up” methods)², although losing control in the spatial arrangement of the self-assembled structures. This limits the freedom of modulating the in-plane optical properties, which is crucial in the fabrication of photonic devices³.

Recently, a third route for engineering the in-plane properties of a semiconductor has been demonstrated, by exploiting the effects of hydrogen irradiation in dilute nitrides (in particular in $\text{GaAs}_{1-y}\text{N}_y$)⁴. In these alloys, the substitution of few percents of As atoms by N leads to strong nonlinear effects in the electronic properties. In particular, it causes a giant reduction in the optical band gap⁵. Post-growth irradiation with atomic hydrogen reverses this band-gap change due to the formation of stable N-H complexes that also modify, among other parameters, the crystal lattice constant⁶. Thus, by allowing H incorporation in selected

regions of the sample, it is possible to achieve a spatially tailored modulation of the band-gap energy as well as of the lattice parameter in the growth plane⁴. This can be done by deposition of masks, which impede H diffusion in defined regions of the crystal⁷ (as sketched in Fig. 1a, b). This new route to in-plane band-gap engineering is very promising: indeed, H-opaque masks (HM) can be easily created by electron beam lithography (EBL), providing size uniformity and exact positioning of the nanostructures; moreover, in-plane band-gap profiles are erasable and rewritable since hydrogenation effects are reversible⁸.

For nanophotonics and quantum technologies based on hydrogenated dilute nitrides⁹, a big breakthrough would be to push down this approach to the nanometer scale length. In a proof-of-principle experiment, the realization of site-controlled quantum dots with potential wells small enough to observe quantum confinement has been achieved^{7,10}; modern EBL systems allow one to make HM with a resolution of 10 nm^{11,12}. In order to control fabrication at the nanoscale, the need of a nondestructive high-resolution imaging technique able to visualize the obtained patterns is mandatory. Moreover, such a technique should be able to image individual nanostructures as these may not be identical, especially during the stages of an optimization process. Unluckily, the spatial resolution of optical imaging (micro-PL, micro-Raman) is restricted by the diffraction limit of

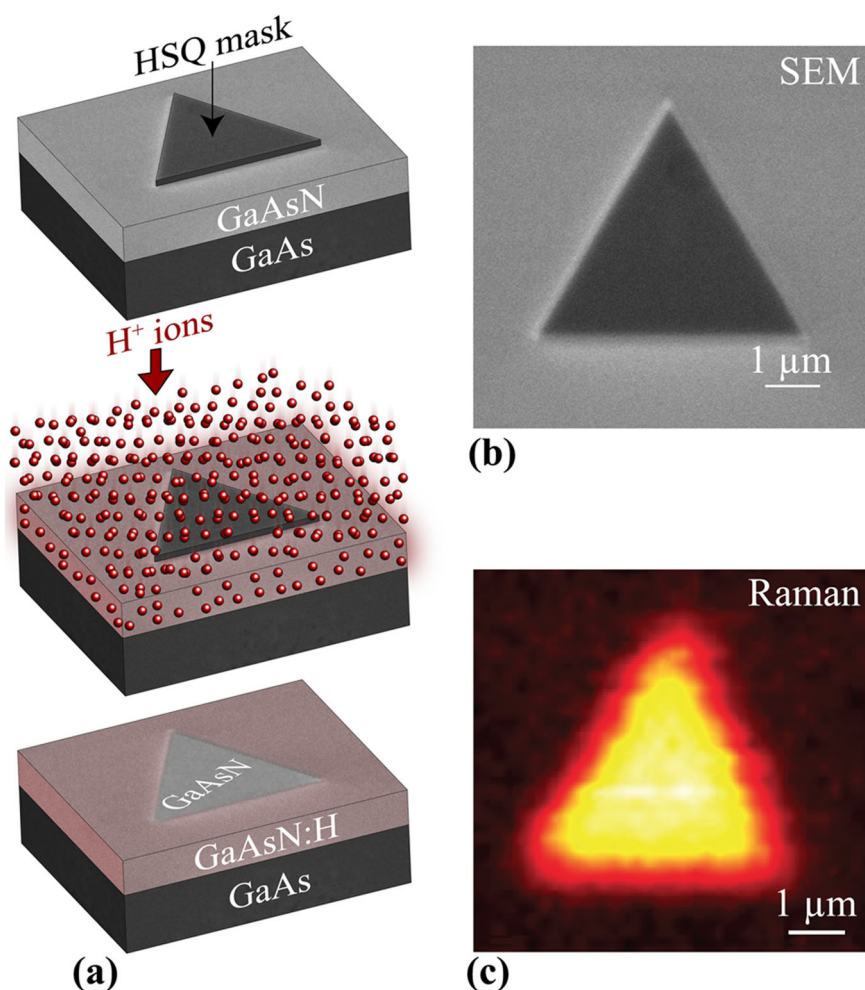


Fig. 1 Sketch of the HM-based fabrication process and pre-characterization. **a** Sketch of the micro-fabrication process described in the “Methods” section, based on the use of lithography-defined hydrogen masks (HM) and H-ions irradiation: after removal of the mask a triangular $\text{GaAs}_{1-y}\text{N}_y$ microstructure is left in the epilayer, surrounded by hydrogenated $\text{GaAs}_{1-y}\text{N}_y$ regions of larger out-of-plane lattice parameter. **b** Scanning electron microscopy (SEM) image of the HM used in the process (an equilateral triangle of $\sim 5 \mu\text{m}$ side), prior to mask removal. **c** Micro-Raman color intensity map of the triangular $\text{GaAs}_{0.991}\text{N}_{0.009}$ object fabricated as sketched in **a**.

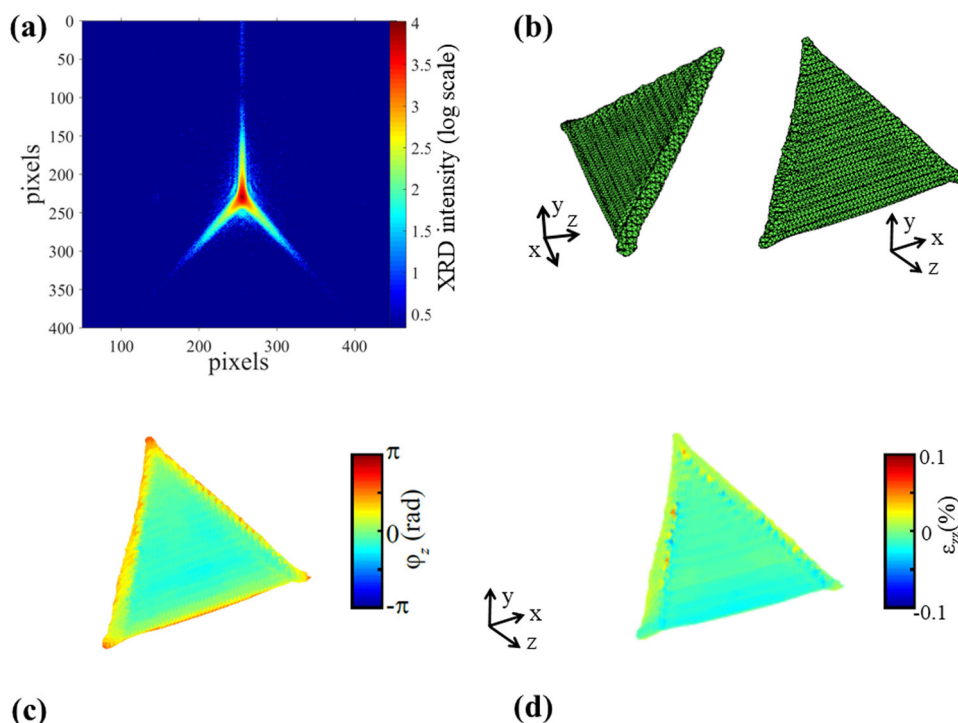


Fig. 2 BCDI results for a structure obtained with the 5- μm -side triangular mask and using the $y = 0.9\%$ $\text{GaAs}_{1-y}\text{N}_y$ epilayer. **a** XRD pattern at the peak of the [004] $\text{GaAs}_{1-y}\text{N}_y$ rocking curve taken by a 13- μm -pixel size CCD camera. Intensity color map (right side) is in logarithm scale given as power of 10. **b** Reconstruction of the amplitude of the complex density function giving the 3D shape of the fabricated microstructure; the two renderings use isosurfaces equal to 50% of the amplitude maximum. The reconstructed triangle looks flat since the thickness of the original $\text{GaAs}_{1-y}\text{N}_y$ epilayer (200 nm) is much smaller than the object lateral dimensions. Resolution of the reconstructed image is about 85 nm, pixel size is 51 nm. **c** Reconstruction of the phase of the complex density function, producing a 3D map of the out-of-plane atom displacement; the phase is represented by the phase values that intersect the amplitude isosurface obtained at 50% of the amplitude maximum. The color scale has radians units, phase zero corresponding to the strain level of the $\text{GaAs}_{1-y}\text{N}_y$ alloy pseudomorphically grown on the GaAs substrate. **d** Reconstruction of the out-of-plane strain (ϵ_{zz}) calculated as the gradient of the out-of-plane atom displacement field (u_z) along the momentum transfer direction; the strain is represented by the strain values that intersect the amplitude isosurface obtained at 50% of the amplitude maximum, the color scale is in percent. The displacement u_z is related to the phase Φ_z through the relation $\Phi_z = 4 \times (2\pi/a_z^{\text{GaAsN}}) \times u_z$, where a_z^{GaAsN} is the out-of-plane lattice parameter of $\text{GaAs}_{1-y}\text{N}_y$. In the Cartesian axis representation “z” indicates the vertical direction, “y” the direction of the x-ray beam, “x” the direction transverse to the beam; the same representation is used in all figures. The full 3D reconstructed complex density function is available upon request from the authors as a Matlab data file.

the laser light used and it is not better than 1 μm ; a micro-Raman color intensity map of a structure fabricated using a triangular HM of 5 μm lateral dimension is shown in Fig. 1c. This resolution is not sufficient to demonstrate the regularity and geometrical sharpness of the microstructures obtained; furthermore, micro-PL and micro-Raman do not give direct access to the strain distribution in the microstructures, especially along the growth axis.

Electron microscopies such as transmission (TEM), scanning, and scanning tunneling would be not suitable in this case because of the low contrast between the hydrogenated and non-hydrogenated sample sections. Furthermore, the nanostructures need to be buried below the surface to obtain high optical quality in devices and controlled confinement along the growth direction for specific applications. Moreover, the preparation of thin samples for TEM would require a processing that can introduce additional strain. An unusually large field of view would also be required in TEM to visualize structures of $\sim 5 \mu\text{m}$ lateral size.

In this article, we show how these issues can be efficiently tackled using the coherent x-ray diffractive imaging (CDI) technique. CDI^{13–15} is a lensless imaging methodology at nanometer spatial resolution, being it not limited by the size of the x-ray beam. It can be used to reconstruct three-dimensional (3D) electron density maps both in biology^{16,17} and materials science^{18,19}. The detailed 3D shape of micro/nanocrystals can be

reconstructed from the oversampled intensity distribution around a Bragg diffraction spot, performing a rocking curve²⁰. Moreover, Bragg CDI (BCDI) gives access to the 3D crystalline lattice distortions and, therefore, to the strain distribution, in the direction of the reciprocal lattice vector chosen^{21,22}. BCDI was used, for example, for imaging dislocation dynamics during phase transformations²³ and Pt nanocrystals deformation during catalytic methane oxidation²⁴. However, the enormous potential of BCDI in the non-destructive imaging of buried, solid-state nanostructures to be used in functional devices, which represents one of the driving forces for the upgrade of the main synchrotron facilities worldwide²⁵, has not been fully exploited yet. The slow progress is related to some technical issues in the imaging of highly strained epitaxial nanostructures: first, the proximity of the substrate Bragg peak and the scattering along the crystal truncation rod produce a background signal that can overlap the diffraction signal from the nanostructure, and second the substrate strongly influences the strain state of the nanostructures. It has been reported that in these conditions, and especially for relatively large nano- and microstructures, reconstructions often do not converge²⁶ or the use of additional direct space constraints in the reconstruction algorithms is needed to obtain convergence²⁷.

Nevertheless, since the contrast producing the image in BCDI derives from the diffraction of a specific crystal structure, it is in

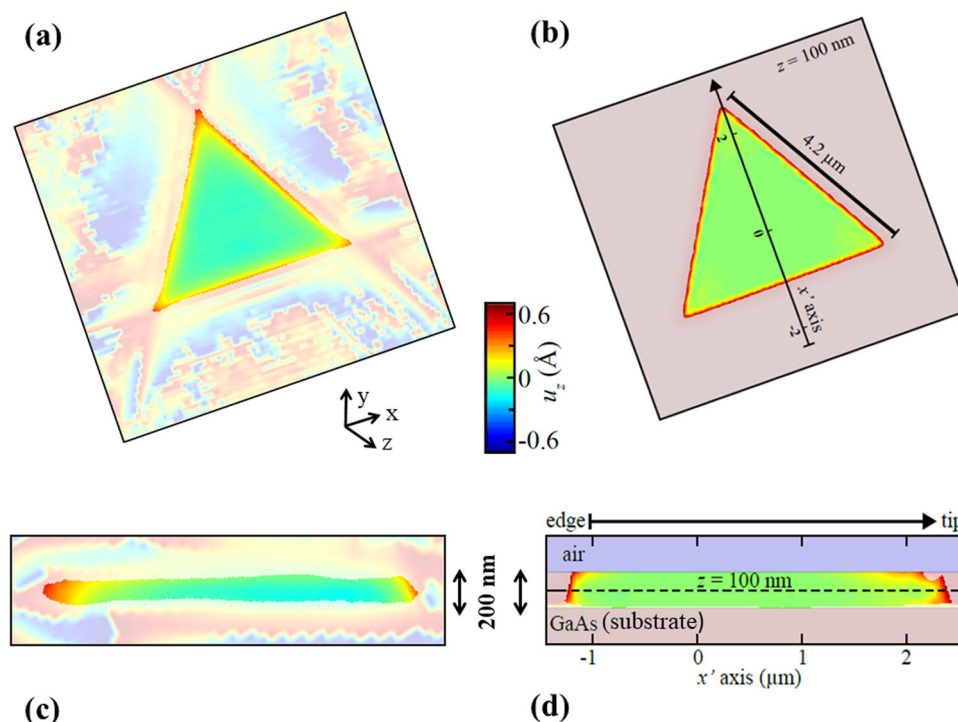


Fig. 3 Comparison between BCDI results and FEA simulations for a triangular structure obtained with the 5- μm -side mask. **a** 2D slice through the 3D reconstructed out-of-plane atom displacement along a plane parallel to the micro-triangle surface and bisecting its thickness (i.e., at $z = +100$ nm from the substrate upper face), the bright area is delimited by the intersection with the isosurface used in Fig. 2b; similar images (not shown) are obtained cutting with parallel planes at different heights. The displacement u_z is related to the phase Φ_z through the relation $\Phi_z = 4 \times (2\pi/a_z^{\text{GaAsN}}) \times u_z$, where a_z^{GaAsN} is the out-of-plane lattice parameter of $\text{GaAs}_{1-y}\text{N}_y$; the color scale is in Å. **b** FEA simulation corresponding to the displacement map of **a**, obtained as described in the “Methods” section and in the Supplementary FEA section, color scale is in Å. **c** Displacement map obtained cutting the triangle with a plane perpendicular to the surface, and passing by one vertex and bisecting the opposite edge, the vertex is at the right of the image, the substrate-side at the bottom. **d** FEA simulation corresponding to the displacement map of **c**. The full amplitude and displacement volumes simulated by FEA are available upon request from the authors.

principle possible to image micro- or nanostructures grown on a substrate or embedded in a matrix, which would not be possible with classical imaging methods. Successful reconstructions have been obtained on other strained epitaxial systems such as silicon-on-insulator and SiGe nanostructures^{28,29}. In the present study, we show that good quality 3D electron density and strain maps can be extracted by BCDI in an even more challenging case, where the $\text{GaAs}_{0.991}\text{N}_{0.009}$ planar structures under investigation are directly grown on the substrate, and not supported by amorphous oxide buffer layers. Here, the contrast producing the images is created by the tiny separation of the Bragg peak of $\text{GaAs}_{0.991}\text{N}_{0.009}$ from the one of the GaAs substrate (0.37% lattice parameter mismatch) and the one of the surrounding hydrogenated $\text{GaAs}_{0.991}\text{N}_{0.009}$ ($\text{GaAs}_{0.991}\text{N}_{0.009}\text{:H}$) walls (0.49% mismatch)³⁰.

Results

BCDI and FEA simulations of $\text{GaAs}_{0.991}\text{N}_{0.009}$ microstructures.

Figure 2a shows the distribution of the scattered intensity around the $\text{GaAs}_{1-y}\text{N}_y$ [004] reflection (Bragg angle $\sim 31^\circ$) by the triangular feature of Fig. 1c, when illuminated by a coherent x-ray beam; the threefold symmetry comes from the fact that the diffraction pattern is given by the square modulus of the Fourier transform (FT) of the function describing the external shape of the micro-object³¹. Figure 2b shows the amplitude of the complex shape function (the physical $\text{GaAs}_{1-y}\text{N}_y$ electron density) reconstructed using the retrieval procedure described in the experimental section. The resolution of the reconstructed 3D

image is about twelve times better than that obtained by optical imaging (micro-PL and micro-Raman), thus allowing us to prove the sharpness of the manufactured profiles. In Fig. 2c, we show the phase of the complex shape function, which is proportional to the atom displacements projected onto the reciprocal lattice vector, related to the out-of-plane strain for a [004] Bragg reflection. We apprehend from the figure that the atom displacement is rather constant in the inner micro-triangle and the only notable variations are observed at the borders with the $\text{GaAs}_{1-y}\text{N}_y\text{:H}$ barriers, characterized by a larger lattice parameter. In Fig. 2d, we directly show the out-of-plane strain ϵ_{zz} calculated as the gradient of the out-of-plane displacement field (u_z) on the momentum transfer direction³². Note that the values of ϵ_{zz} are rather small far from the contours, despite the microstructure is pseudomorphically strained to the substrate, since in our representation the “zero level” for strain is given by the $\text{GaAs}_{1-y}\text{N}_y$ structure and not by the GaAs substrate.

In Fig. 3 the out-of-plane displacement maps extracted by BCDI are compared with finite element analysis (FEA) simulations performed as described in the “Methods” section. Here, the displacement volume is bisected by a plane parallel to the triangle surface to visualize an internal section. The simulations confirm the experimental results: they show a flat strain distribution in the inner triangle and a quite sharp variation only in proximity of the borders. Moreover, the calculated out-of-plane displacement field (u_z) is in quantitative agreement with the reconstruction, demonstrating the reliability of the imaging method. In Fig. 3c one can note the sharpness of the lateral

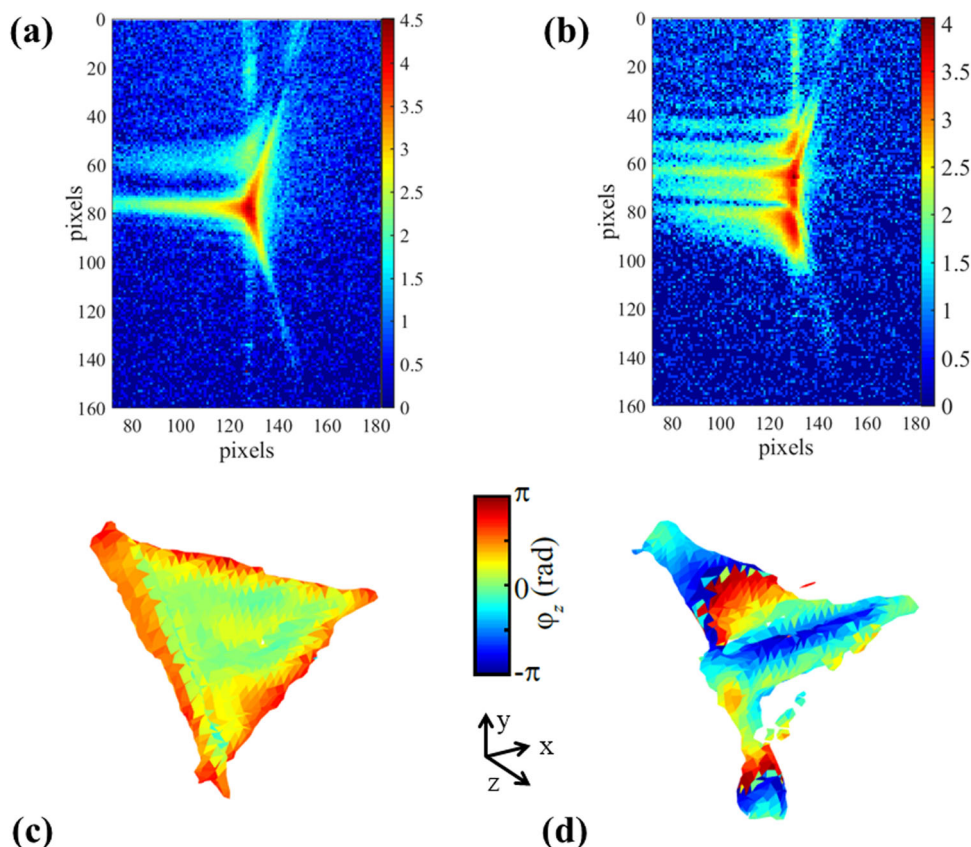


Fig. 4 BCDI of microstructures with less uniform strain distribution obtained with 5- μm -side triangular HM. **a, b** XRD patterns taken at the peak of the [004] $\text{GaAs}_{1-y}\text{N}_y$ rocking curve. **c, d** Relative reconstructed phase maps represented by the phase values that intersect the amplitude isosurfaces equal to 40% and 30% of the amplitude maximum, respectively. Intensity color map of the XRD patterns has logarithm scale given as power of 10, phases have radians units. Resolution of the reconstructed images is about 83 and 90 nm, respectively; pixel size is 72 nm. Note that the XRD patterns are differently oriented with respect to the one of Fig. 2a due to a different orientation of the micro-triangles with respect to the x-ray beam. In the Cartesian axis representation “z” indicates the vertical direction, “y” the direction of the x-ray beam, “x” the direction transverse to the beam. The full 3D reconstructed complex density functions for the two microstructures are available upon request from the authors as Matlab data files.

profile of the $\sim 200\text{-nm}$ -thick layer, also well reproduced by the simulations (Fig. 3d), which would be hard to probe experimentally without the use of BCDI.

BCDI of microstructures with nonuniform strain distribution.

The agreement between BCDI and FEA calculations in Fig. 3 indicates that the fabricated microstructure has high strain uniformity; however, the investigation of several microstructures reveals that statistically this is not always the case. In fact, some of the micro-triangles exhibit more complex strain distributions and/or structural relaxation, as the ones shown in Fig. 4. For these microstructures, the 2D XRD patterns (Fig. 4a, b) show one or more repetitions of the equilateral triangle FT; such replicas speak for a distribution of the lattice parameter in the direction perpendicular to the growth plane. When in the XRD pattern the intensity of the repetitions is weaker than the one of the main triangle FT (about 2 orders of magnitude), upon reconstruction we observe a nonuniform distribution of the out-of-plane strain even far from the micro-triangle sides (Fig. 4c); however, the phase variation remains limited and does not exceed π . On the other hand, when the structural relaxation in the micro-object is more significant and the intensity of the repetitions is comparable to the one of the main triangle FT (<1 order of magnitude difference) (Fig. 4b), the reconstructed phase map is more disordered (Fig. 4d), showing phase wraps representative of larger atom displacements (a phase wrap is a signature of a

displacement larger than the lattice spacing). When the strain variation inside the micro-object is sufficiently large to produce phase wraps, the reconstruction of the 3D shape of the object is more complicated and we cannot exclude the presence of artefacts. Nevertheless, Fig. 4 demonstrates the potential of BCDI for direct evaluation of the structural quality of the single microstructures produced via the new patterning process; such an evaluation could be hardly carried out with more conventional microscopy techniques.

BCDI and FEA of sub-microscopic $\text{GaAs}_{0.958}\text{N}_{0.042}$ structures.

In order to explore the possibility to drive the new fabrication process down to the nanoscale, we performed BCDI on microstructures produced with HM of 500 nm side (Fig. 5a). From the $\text{GaAs}_{0.958}\text{N}_{0.042}$ [004] XRD pattern shown in Fig. 5b, distinguishing the threefold symmetry of a triangle FT is not obvious any more. A triangle-like shape is nevertheless recovered after reconstruction, as shown in the phase map of Fig. 5c. Surprisingly, phase variations in this map remain rather small (± 2 radians) when compared with the micrometric structures of Figs. 2–4, even at the nano-triangle contours. This occurs in spite of the higher N concentration in the $\text{GaAs}_{0.958}\text{N}_{0.042}$ triangle, and of the consequent larger lattice mismatch with the $\text{GaAs}_{0.958}\text{N}_{0.042}\text{-H}$ walls. This is also confirmed by FEA simulations (Fig. 5d). This result demonstrates the possibility of fabricating highly strained nanostructures of arbitrary shape.

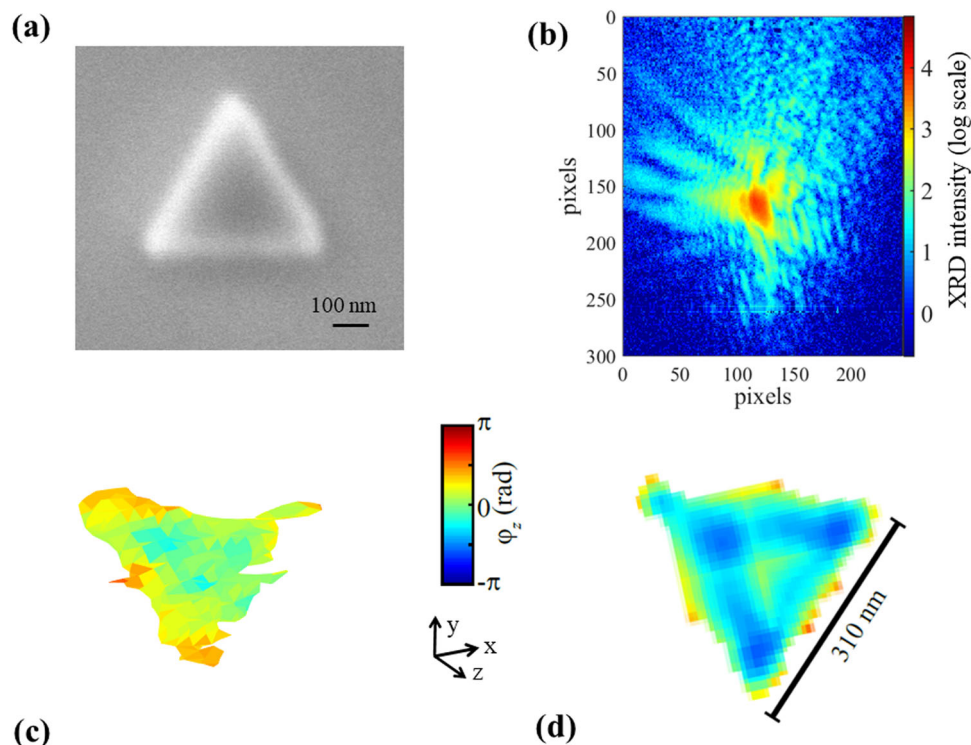


Fig. 5 BCDI and FEA of a structure fabricated with a 500-nm-side triangular mask and using the $y = 4.2\%$ $\text{GaAs}_{1-y}\text{N}_y$ epilayer. **a** SEM image of the 500-nm-side hydrogen-opaque mask used to produce the $\text{GaAs}_{1-y}\text{N}_y$ triangular structure. **b** XRD pattern taken at the peak of the $\text{GaAs}_{1-y}\text{N}_y$ [004] rocking curve by a 55- μm -pixel MAXIPIX 2D detector. Intensity color map (right side) is in logarithm scale given as power of 10. **c** Reconstruction of the phase of the complex density function, producing a 3D map of the out-of-plane strain; the phase is represented by the phase values that intersect the amplitude isosurface obtained at 35% of the amplitude maximum, the color scale has radians units. Resolution of the reconstructed image is about 25 nm, pixel size is 22 nm. **d** FEA simulation corresponding to the phase rendering of **c**.

However, the blurring of the reconstructed triangle profile suggests that the precision of the fabrication process still needs improvement; this consideration is possible thanks to the high resolution (~ 25 nm) of the reconstructed image.

Discussion

We can say that the quality of all reconstructions shown is generally good, especially in the light of the pseudomorphic character of our micro- and nanostructures, the direct epitaxy on a resembling crystalline substrate, the structure size, and the absence of additional direct space constraints in the reconstruction algorithms used. The problem of the scattering background from the substrate tail and along the truncation rod, which often affects similar experiments on highly strained epitaxial systems²⁶, has been dealt with by choosing N concentrations high enough to obtain a sufficient separation of the $\text{GaAs}_{1-y}\text{N}_y$ peak from the substrate one for the [004] reflection, limiting in this way the contribution of the background on the signal diffracted from the sample.

In conclusion, we showed the high potential of strain-sensitive BCDI for an insight into the micro- and nanofabrication process of novel engineered components for photonic devices. We demonstrated that the HM-based patterning of dilute nitrides is able to produce regular and sharp geometrical objects on a few-micron scale, with uniform strain distribution in the inner microstructure. When the microstructure fabrication is successful, the strain-field distribution varies only at the micro-object contour, in agreement with FEA calculations; imaging this strain variation is key for applications in, e.g., light-polarization control³³. BCDI also enables a quality evaluation of the

microstructures produced, spotting more complex strain distribution wherever the process is not optimal. Finally, we showed that the BCDI resolution is sufficient to image shape and strain distribution in objects with submicron dimensions; in this case the strain distribution is narrow despite the larger lattice mismatch between $\text{GaAs}_{1-y}\text{N}_y$ and $\text{GaAs}_{1-y}\text{N}_y\text{:H}$. This result paves the way for the realization of smaller unrelaxed nanostructures, by improving the precision of the EBL-based mask fabrication and the control of the hydrogen diffusion profile. It is worth remarking here that the BCDI technique will become even more powerful with synchrotron upgrades in the near future²⁵. For the SOLEIL storage ring, for example, an increase of about two orders of magnitudes in brilliance, transverse coherence, and coherent photon flux is foreseen; this will allow the study of smaller objects down, at least, to a few tens of nm. The identification of a strain-sensitive technique able to visualize at the nanoscale the patterns obtained by spatially selective hydrogenation represents the first step toward fulfilling the true potential of this fabrication process. This will enable the fine-tuning of the optical properties of quantum emitters via tailoring the nanostructures potential profile, hence the realization of complex nanophotonic devices such as single and entangled-photon sources, routers, switches, and delay lines.

Methods

Sample fabrication. The micro- and nanostructures under study were obtained by two $\text{GaAs}_{1-y}\text{N}_y/\text{GaAs}$ epilayers: the first with $y \sim 0.9\%$ and thickness ~ 200 nm and the second with $y \sim 4.2\%$ and thickness ~ 50 nm, both pseudomorphic to the GaAs substrate. Hydrogenation was performed at 300 °C by irradiating the samples with an H-dose of 2×10^{18} ions/cm² (for the $y \sim 0.9\%$ sample) and 4×10^{18} ions/cm² (for the $y \sim 4.2\%$ sample), by means of a Kaufman ion source. The samples were patterned by using triangular HM of side equal to 5 μm or 500 nm prior to

hydrogenation (the out-of-plane dimension of the GaAs_{1-y}N_y micro- and nanostructures is set by the epilayer thickness). In order to have better statistics on the reliability of the fabrication process, arrays of microstructures covering a large area of the epilayers were created maintaining a separation of 200 μm along the two in-plane directions between two adjacent microstructures, which was sufficient to illuminate single micro-objects using a coherent x-ray beam. EBL-defined masks were patterned out of a H-opaque, hydrogen silsesquioxane (HSQ) negative resist using a Vistec EBPG 5HR EBL system working at 100 kV. After the hydrogenation, and before performing the sample analysis, the HSQ masks were removed by chemical etching in an aqueous solution of potassium borates and potassium hydroxide.

Optical microscopy characterization. The experimental setup for micro-Raman measurements (Fig. 1c) comprised a He–Ne laser ($\lambda = 633$ nm), an XY linear positioning stage, an optical confocal microscope system, a spectrometer with 1200 groves/mm gratings, equipped with a charge-coupled device (CCD) photodetector. The laser beam was focused to a diameter $d \approx 1$ μm using a 100× objective and the micro-Raman spectra were measured at low power ($P \sim 0.1$ mW) to avoid lattice heating and hydrogen removals. The Raman map was obtained by plotting the micro-Raman intensity at 290 cm⁻¹ corresponding to the main longitudinal optical LO_T-mode of GaAsN.

Coherent x-ray diffraction (CXD) imaging. CDI was performed in Bragg geometry at the CRISTAL and SIRIUS beamlines of SOLEIL synchrotron (Saint-Aubin, France) selecting the [004] crystal plane reflection of GaAs_{1-y}N_y. A sketch showing the geometrical configuration used in the experiments is provided in Supplementary Fig. 1. We selected for all experiments incident photon energy of 8.5 keV by using a Si-(111) monochromator (energy resolution better than 1 eV). The incident x-ray beam was delimited by high precision slits in order to select its coherent part and produce a spot on the sample slightly larger than the microstructure under analysis (10 μm² for the objects obtained with the 5 μm-side HM), as required by the reconstruction procedures employed. The photon flux on the x-ray spot was about 3×10^7 ph/s. As for the objects manufactured with the 500 nm mask, we used a system of gold Fresnel zone plate lenses (FZP) focusing the coherent x-ray beam to a spot of about 1×2 μm² (HxV). The FZP used have 20 cm focal length, 100 nm outer zone, 295 μm diameter, and 1.4 μm thickness. The flux on the x-ray spot was about 10⁸ ph/s. Two different 2D position-sensitive detectors were used to collect the diffraction pattern: an ANDOR back-illuminated CCD camera with pixel size = 13 μm and a MAXIPIX hybrid pixel detector with pixel size = 55 μm. The sample-detector distance was 1.77 and 2.10 m for the big and small triangle, respectively. The 3D CXD patterns were acquired as rocking curves of the sample, rotating in 65 steps of 0.0015° about a horizontal axis for the 5 μm objects and in 101 steps of 0.003° for the 500 nm objects. For the 5 μm structures we accumulated 200 images (~1 s per image) per step in order to record the diffraction pattern, while for the 500 nm structures we accumulated 50 images per step. The CXD patterns were inverted to images with a phase retrieval algorithm, following support-based phasing using a version of Fienup's hybrid input–output³⁴ and error reduction (ER) algorithm^{21,22,35}. We also used a custom version of the “shrink wrap” method³⁶ to determine the support region of the object. The resolution of the reconstructions (given in the figure captions along with the pixel size) has been quantified by performing linecuts at the surface of the reconstructed crystals; a Gaussian distribution has been fitted to the derivative of the edge and the average σ width of the Gaussians obtained from linecuts along the three Cartesian directions is retained as resolution value³⁷. Similar values have been obtained by measuring the radially averaged phase retrieval transfer function (PRTF) and taking the spatial frequency point where the PRTF drops below 1/e, where e is the Euler's number^{38,39}.

FEA simulations. As also discussed in the Supporting Information, two separate rounds of FEA simulations are required to compute the effects of spatially selective H irradiation on the structural properties of a GaAs_{1-y}N_y/GaAs epilayer. As detailed in Ref. 33, the first round of simulations is based on the diffusion-reaction equations introduced in Ref. 40, and it allows us to model the process of H diffusion in a GaAs_{1-y}N_y sample partially covered with a H-opaque triangular mask. Provided that the simulations are correctly calibrated—by making sure that the time required to fully passivate the epilayer matches the one observed in the experiments—the solutions to these equations yield accurate concentration “maps” for the N-H complexes responsible for N passivation (see Supporting Information) after a given hydrogenation time. In turn, these concentration maps allow us to directly quantify the expansion locally induced in every point of the GaAs_{1-y}N_y lattice by the presence of N-H complexes. This information provides us with the initial conditions required by the second round of FEA simulations, which enables us to evaluate the six components of the (anisotropic) strain tensor—and, thus, the lattice parameter and the atomic displacements—in every point of the computational domain. As illustrated in Figs. 3 and 5, the displacement in the z direction can be directly compared with BCDI data, providing very useful information both on the reliability of this modern characterization technique and on the performance of our nanofabrication method. As for the boundary conditions used for the determination of the strain, the computational domain was a $15 \times 15 \times t$ slab, where

t is the thickness of the GaAsN epilayer under consideration. Continuous periodic boundary conditions were imposed in-plane, whereas a fixed constraint was applied to the bottom surface of the slab, so as to simulate the effect of the substrate. Having obtained the concentrations of all the N-nH complexes present in the sample from our simulation of the H diffusion process, we can compute the relaxed lattice parameter for the GaAsN:H alloy in every point of the epilayer, a , based on the equation

$$a = a_{\text{GaAs}} + b_{\text{N3H}} \times n_{\text{N3H}} - b_{\text{N}} \times n_{\text{N}}$$

Here, a_{GaAs} is the lattice parameter of GaAs, n_{N} and n_{N3H} are the concentrations of unpassivated N atoms and of N-3H complexes, respectively, while $b_{\text{N3H}} = 0.46 \text{ \AA}^4$ and $b_{\text{N}} = 1.12 \text{ \AA}^4$ are the coefficients giving the effects of N-3H and N on the lattice constant. We can thus estimate the variation of a (with respect to a_{GaAs}) in every point of the epilayer, which can then be included among the initial conditions of our FEM simulation as a local expansion/contraction of the lattice. The computed strain distribution stems directly from this initial lattice deformation, combined with the presence of the fixed constraint at the bottom of the epilayer.

Data availability

The data supporting the findings of this study are available from the corresponding author upon reasonable request.

Received: 22 October 2019; Accepted: 17 March 2020;

Published online: 24 April 2020

References

- Jöns, K. D. et al. Triggered indistinguishable single photons with narrow line widths from site-controlled quantum dots. *Nano Lett.* **13**, 126–130 (2013).
- Bimberg, D., Grundmann, M. & Ledentsov, N. N. *Quantum Dot Heterostructures* (Wiley, Chichester, 1998).
- Englund, D. et al. Deterministic coupling of a single nitrogen vacancy center to a photonic crystal cavity. *Nano Lett.* **10**, 3922–3926 (2010).
- Birindelli, S. et al. Single photons on demand from novel site-controlled GaAsN/GaAsN:H quantum dot. *Nano Lett.* **14**, 1275–1280 (2014).
- Henini, M. *Dilute Nitride Semiconductors* (Elsevier, Amsterdam, 2005).
- Ciatto, G. *Hydrogenated Dilute Nitride Semiconductors: Theory, Properties, and Applications* (Pan Stanford, Singapore, 2015).
- Trotta, R. et al. Fabrication of site-controlled quantum dots by spatially selective incorporation of hydrogen in Ga(AsN)/GaAs heterostructures. *Adv. Mater.* **23**, 2706–2710 (2011).
- Felici, M. et al. In-plane bandgap engineering by modulated hydrogenation of dilute nitride semiconductors. *Adv. Mater.* **18**, 1993–1997 (2006).
- Pettinari, G., Felici, M., Biccari, F., Capizzi, M. & Polimeni, A. Site-controlled quantum emitters in dilute nitrides and their integration in photonic crystal cavities. *Photonics* **5**, 10 (2018).
- Biccari, F. et al. Site-controlled single-photon emitters fabricated by near-field illumination. *Adv. Mater.* **30**, 1705450 (2018).
- Mohan, A. et al. Record-low inhomogeneous broadening of site-controlled quantum dots for nanophotonics. *Small* **6**, 1268–1272 (2010).
- Pettinari, G. et al. A lithographic approach for quantum dot-photonic crystal nanocavity coupling in dilute nitrides. *Microelectron. Eng.* **174**, 16–19 (2017).
- Sayre, D. *Imaging Processes and Coherence in Physics*, Vol. 112 (eds Schlenker, A. et al.), 229–235 (Springer, 1980).
- Miao, J. W., Charalambous, P., Kirz, J. & Sayre, D. Extending the methodology of X-ray crystallography to allow imaging of micrometre-sized non-crystalline specimens. *Nature* **400**, 342–344 (1999).
- Chapman, H. N. & Nugent, K. A. Coherent lensless X-ray imaging. *Nat. Photonics* **4**, 833–839 (2010).
- Nishino, Y., Takahashi, Y., Imamoto, N., Ishikawa, T. & Maeshima, K. Three-dimensional visualization of a human chromosome using coherent X-ray diffraction. *Phys. Rev. Lett.* **102**, 018101 (2009).
- Jiang, H. et al. Quantitative 3D imaging of whole, unstained cells by using X-ray diffraction microscopy. *PNAS* **107**, 11234–11239 (2010).
- Barty, A. et al. Three-dimensional coherent X-ray diffraction imaging of a ceramic nanofoam: determination of structural deformation mechanisms. *Phys. Rev. Lett.* **101**, 055501 (2008).
- Ulvestad, A. et al. Single particle nanomechanics in operando batteries via lensless strain mapping. *Nano Lett.* **14**, 5123–5127 (2014).
- Williams, G. J., Pfeifer, M. A., Vartanyants, I. A. & Robinson, I. K. Three-dimensional imaging of microstructure in Au nanocrystals. *Phys. Rev. Lett.* **90**, 175501 (2003).
- Pfeifer, M. A., Williams, G. J., Vartanyants, I. A., Harder, R. & Robinson, I. K. Three-dimensional mapping of a deformation field inside a nanocrystal. *Nature* **442**, 63–66 (2006).

22. Robinson, I. K. & Harder, R. Coherent X-ray diffraction imaging of strain at the nanoscale. *Nat. Mater.* **8**, 291–298 (2009).
23. Ulvestad, A. et al. Three-dimensional imaging of dislocation dynamics during the hydriding phase transformation. *Nat. Mater.* **16**, 565–571 (2017).
24. Kim, D. et al. Active site localization of methane oxidation on Pt nanocrystals. *Nat. Commun.* **9**, 3422 (2018).
25. Eriksson, M. The multi-bend achromat storage rings. *AIP Conf. Proc.* **1741**, 020001 (2016).
26. Diaz, A. et al. Imaging the displacement field within epitaxial nanostructures by coherent diffraction: a feasibility study. *New J. Phys.* **12**, 035006 (2010).
27. Minkevich, A. A. et al. Inversion of the diffraction pattern from an inhomogeneously strained crystal using an iterative algorithm. *Phys. Rev. B* **76**, 104106 (2007).
28. Xiong, G., Moutanabbir, O., Reiche, M., Harder, R. & Robinson, I. Coherent X-ray diffraction imaging and characterization of strain in silicon-on-insulator nanostructures. *Adv. Mater.* **26**, 7747–7763 (2014).
29. Holt, M. V. et al. Strain imaging of nanoscale semiconductor heterostructures with X-ray bragg projection ptychography. *Phys. Rev. Lett.* **112**, 165502 (2014).
30. Ciatto, G. et al. Synchrotron x-ray diffraction study of micro-patterns obtained by spatially selective hydrogenation of GaAsN. *Appl. Phys. Lett.* **106**, 051905 (2015).
31. Robinson, I. K., Vartanyants, I. A., Williams, G. J., Pfeifer, M. A. & Pitney, J. A. Reconstruction of the shapes of gold nanocrystals using coherent X-ray diffraction. *Phys. Rev. Lett.* **87**, 195505 (2001).
32. Cherukara, M. J. Three-dimensional X-ray diffraction imaging of dislocations in polycrystalline metals under tensile loading. *Nat. Commun.* **9**, 3776 (2018).
33. Felici, M. et al. Nanoscale tailoring of the polarization properties of dilute-nitride semiconductors via H-assisted strain engineering. *Phys. Rev. Appl.* **2**, 064007 (2014).
34. Fienup, J. R. Phase retrieval algorithms: a comparison. *Appl. Opt.* **21**, 2758–2769 (1982).
35. Clark, J. N. et al. Three-dimensional imaging of dislocation propagation during crystal growth and dissolution. *Nat. Mater.* **14**, 780 (2015).
36. Marchesini, S. et al. X-ray image reconstruction from a diffraction pattern alone. *Phys. Rev. B* **68**, 140101 (2003).
37. Dzhibaev, D. et al. Bragg coherent x-ray diffractive imaging of a single indium phosphide nanowire. *J. Opt.* **18**, 064007 (2016).
38. Chapman, H. N. et al. High-resolution ab initio three-dimensional x-ray diffraction microscopy. *J. Opt. Soc. Am. A* **23**, 1179–1200 (2006).
39. Cherukara, M. J., Cha, W. & Harder, R. J. Anisotropic nano-scale resolution in 3D Bragg coherent diffraction imaging. *Appl. Phys. Lett.* **113**, 203101 (2018).
40. Trotta, R. et al. Hydrogen diffusion in GaAs_{1-x}N_x. *Phys. Rev. B* **80**, 195206 (2009).
41. Bisognin, G. et al. Hydrogen-nitrogen complexes in dilute nitride alloys: origin of the compressive lattice strain. *Appl. Phys. Lett.* **89**, 061904 (2006).
42. Bisognin, G. et al. Determination of lattice parameter and of N lattice location in In_xGa_{1-x}NyAs_{1-y}/GaAs and GaNyAs_{1-y}/GaAs epilayers. *J. Appl. Phys.* **95**, 48–56 (2004).

Acknowledgements

This work benefited from the SOLEIL beam time allocations No. 20131027 and No. 20141387 (CRISTAL beamline) and in-house research time (SIRIUS beamline). We

thank Synchrotron SOLEIL for general facilities placed at our disposal; we are grateful for technical support by F. Legrand and N. Aubert. We acknowledge S. Rubini, F. Martelli, and L. Grenouillet for providing the GaAsN samples. G. P., M. F., and A. Po. acknowledge funding from the Italian MIUR (under FIRB project DeLIGHTeD, Protocollo RBFR12RS1W). A. Po. and M. F. acknowledge funding from the Regione Lazio programme “Progetti di Gruppi di ricerca” legge Regionale n. 13/2008 (SINFONIA project, prot. n. 85-2017-15200) via LazioInnova spa. A. Pa. acknowledges the support of the Engineering and Physical Sciences Research Council (grant number EP/J015296/1).

Author contributions

F. B. played the main role in carrying out the BCDI experiments and image reconstructions from the diffraction patterns. G. P. fabricated the micro- and nanostructure by EBL-defined hydrogen masking and participated in most of the experiments. N. B. performed the optical characterization and participated in the first CDI experiment. M. F. took care of the FEA simulations. J. N. C. wrote the software used for the CDI reconstructions. S. R. helped during the experiments at the CRISTAL beamline. A. Pa. participated in optical characterization and analysis. A. Po. made the hydrogenation of the samples. G. C. conceived the project, participated in all experiments, helped in CDI data analysis, and played the main role in the redaction of the manuscript. All co-authors participated in the discussion and interpretation of the results.

Competing interests

The authors declare no competing interests.

Additional information

Supplementary information is available for this paper at <https://doi.org/10.1038/s43246-020-0021-6>.

Correspondence and requests for materials should be addressed to G.C.

Reprints and permission information is available at <http://www.nature.com/reprints>

Publisher's note Springer Nature remains neutral with regard to jurisdictional claims in published maps and institutional affiliations.



Open Access This article is licensed under a Creative Commons Attribution 4.0 International License, which permits use, sharing, adaptation, distribution and reproduction in any medium or format, as long as you give appropriate credit to the original author(s) and the source, provide a link to the Creative Commons license, and indicate if changes were made. The images or other third party material in this article are included in the article's Creative Commons license, unless indicated otherwise in a credit line to the material. If material is not included in the article's Creative Commons license and your intended use is not permitted by statutory regulation or exceeds the permitted use, you will need to obtain permission directly from the copyright holder. To view a copy of this license, visit <http://creativecommons.org/licenses/by/4.0/>.

© The Author(s) 2020